J Mater Sci (2018) 53:9755–9770

Metals

Primary dendrite spacing selection during directional solidification of multicomponent nickel-based superalloy: multiphase-field study

Cong Yang[1], Qingyan Xu[1,*], and Baicheng Liu[1]

[1] *Key Laboratory for Advanced Materials Processing Technology, Ministry of Education, School of Materials Science and Engineering, Tsinghua University, Beijing 100084, China*

Received: 4 January 2018
Accepted: 17 March 2018
Published online: 26 March 2018

ABSTRACT

The primary dendrite spacing selection in a multicomponent Ni-based superalloy during directional solidification was systematically studied using two-dimensional phase-field simulations. The alloy thermodynamic and kinetic data were obtained from Pandat software with PanNickel database and directly coupled into the multiphase-field model. All the simulations were performed on a GPU server, and an optimized computing scheme using GPU shared memory was adopted. First, the morphology of the solidification front was studied, and the segregation pattern was investigated and compared with the experimental results. Then, the dendritic spacing distribution under a wide range of pulling velocities V_p (10–500 μm s^{-1}) and temperature gradients G (2–200 K mm^{-1}) was obtained and analyzed. The simulation results agree well with analytical model that the primary dendrite spacing scales as $\Lambda \propto V_p^{-b}G^{-c}$. The coefficient b is near a constant value of 0.38 and varies slightly between 0.34 and 0.42, while coefficient c increases monotonously from 0.27 to 0.56 with the increasing G. The predicted dendritic spacing agrees well with the experimental data, but exhibits a major difference when under very low cooling rate ($R < 0.1$ K s^{-1}). The effect of grain inclination angle θ on the final primary dendritic spacing was also studied, and an abnormal decrease in dendritic spacing was found under low grain orientation where $\theta < 10°$. When the grain inclination angle exceeds 20°, the dendritic spacing increases with θ as the power law.

Introduction

Nickel-based superalloy single-crystal turbine blades, which are produced by directional solidification technique, have been extensively used in advanced aero-engines. The primary dendrite arm spacing (PDAS), as one of the most important microstructure characteristics in superalloy directional solidification, can influence the material's mechanical properties. Up to now, a variety of directional solidification

Address correspondence to E-mail: scjxqy@tsinghua.edu.cn

https://doi.org/10.1007/s10853-018-2236-1

techniques have been developed, such as Bridgman high-rate solidification technique (HRS) [1], liquid metal cooling (LMC) [2] and zone melting liquid metal cooling (ZMLMC) [3]. The different solidification techniques have provided a range of solidification conditions and thus led to a different distribution of primary spacing in superalloy products [3–11].

The variation of dendritic spacing with pulling velocity V_p and thermal gradient G has long been analyzed in classical theories and numerous experiments. In analytical models [12, 13], the primary dendritic spacing Λ observes the power law $\Delta T_0^a V_p^{-b} G^{-c}$, where ΔT_0 is the alloy solidification range, $a = b = 0.25$ and $c = 0.5$. The experimental results found that coefficients b and c do not remain constant under different cooling conditions, and they vary from 0.19 to 0.75 and 0.3 to 0.56, respectively. As for the orientation dependence of the primary dendrite spacing, Gandin et al. [14] proposed a model based on experiments with SCN-3.61 wt% acetone alloy as:

$$\Lambda \propto \Delta T_0^a V_p^{-b} G^{-c} F(\theta) \tag{1}$$

by putting forward an orientation correction

$$F(\theta) = 1 + d[(\cos\theta)^{-e} - 1] \tag{2}$$

From the experiments and analysis, the coefficients they estimated are $d \approx 0.15$ and $e \approx 8$ for range of velocity V_p (20–1000 μm s^{-1}) and temperature gradient G (0.1–10 K mm^{-1}).

The primary spacing in directionally solidified nickel-based superalloy has been studied since 1970s. Quested and McLean [4] investigated four nickel-based superalloy and showed that the Λ was indeed scaling as $V_p^{-0.25} G^{-0.5}$. Schneider et al. [15] used an expression $\Lambda = 147(V_p G)^{-0.3384}$ that has been found to be applicable to a wide range of superalloys. Li [5, 6] presented detailed data on the dependence of primary dendrite arm spacing on a wide range of thermal gradients and solidification velocities, and especially under lower-temperature gradients. Liu [3] used the ZMLMC technique and studied the dendritic spacing under high-temperature gradients up to 1000 K cm^{-1}. Although experiments have been done to investigate the primary spacing of superalloy variation, the parameters of the solidification were mostly not well defined, especially the temperature gradient. In general, there is not a well-accepted expression for the primary dendrite spacing with relationship to temperature gradient and pulling velocity. The coefficients in Eq. (1) seem to vary with solidification conditions according to existing experimental results. Moreover, the systematic investigation of primary spacing distribution under a wide range of solidification conditions has not yet been accomplished.

The phase-field method [16–20], which adopts the concept of diffuse interface, has proven to be a powerful tool to study microstructure evolution in alloy solidification. For the simulation of complex multicomponent technical alloy like superalloy, the link of CALPHAD (CALculation of PHase Diagram) databases with phase-field model has become the common choice. Warnken [21] and Böttger [22] have used the multiphase-field model coupled with thermodynamic database to investigate the dendrite growth and segregation behavior in nickel-based superalloy. However, due to expensive computational cost of calculating multicomponent diffusion, the computational domain is limited and cannot be applied to large-scale superalloy directional solidification simulation. Recently, the GPU (graphical processing unit)-based parallel computing technique has been extensively used in accelerating phase-field computation [23–25]. By applying the GPU parallel computing scheme to phase-field model, it is now possible to study the primary dendrite selection in a multicomponent superalloy.

In this work, the multiphase-field model proposed by Steinbach [18] is adopted, and the software Pandat with PanNi database is used to present realistic superalloy thermodynamic data for multiphase-field model. The computation process is accelerated by a previously developed GPU computing scheme [23], which achieves more than 200 times speed-up ratio compared with that using a single CPU core. The main target of this research is to investigate the primary dendrite spacing in a wide range of pulling velocities (10–500 μm s^{-1}) and temperature gradients (2–200 K mm^{-1}) by large-scale phase-field simulations. The simulation results are analyzed using the analytical model in Eq. (1) and then compared with the experimental results. In addition, the effect of grain inclination angle on the final dendritic spacing is also investigated, and the results are different from the analytical model prediction when under small inclination angles ($\theta < 10°$).

Methods

The directional solidification of the superalloy involves a complex solidification path with coupled heat and multicomponent solute diffusion. The phase-field model for binary alloy with a linearized phase diagram can hardly describe the solidification behavior of the superalloy. The multiphase-field model, which take account the effect of all the individual alloy components, has provided a better choice to simulate the superalloy solidification.

Multiphase-field model

The multiphase-field model used in this work was first proposed by Steinbach and Eiken et al. [18, 19], and the model is able to simulate multicomponent superalloy phase transformations [21]. In this model, all phases are represented by a set of scalar phase fields $\{\phi_\alpha(\vec{x},t)\}$, with the constraint $\sum_{\alpha=1}^{v}\phi_\alpha = 1$. The alloy phase compositions $\{\vec{c}_\alpha(\vec{x},t)\}$ have individual value in each phase and vary smoothly at the phase interfaces. The free energy functional is the integration of local density functional over the domain Ω.

$$F(\{\phi_\alpha\},\{\vec{c}_\alpha\}) = \int_\Omega f(\{\phi_\alpha\},\{\vec{c}_\alpha\}) \tag{3}$$

The density functional is the sum of chemical energy density $f^{\text{chem}}(\{\phi_\alpha\},\{\vec{c}_\alpha\})$ and interface energy density $f^{\text{intf}}(\{\phi_\alpha\})$. For an alloy system with v phases, the free energy density can be expressed as

$$\begin{aligned} f &= f^{\text{intf}}(\{\phi_\alpha\}) + f^{\text{chem}}(\{\phi_\alpha\},\{c_\alpha^k\}) \\ &= \sum_{\alpha=1}^{v}\sum_{\beta=\alpha+1}^{v}\frac{4\sigma_{\alpha\beta}}{v\eta}\left(-\frac{\eta^2}{\pi^2}\nabla\phi_\alpha\nabla\phi_\beta + \phi_\alpha\phi_\beta\right) + \sum_{\alpha=1}^{v}\phi_\alpha f_\alpha(\vec{c}_\alpha) \end{aligned} \tag{4}$$

where $\sigma_{\alpha\beta}$ denotes the interface energy between phase α and phase β in a multiphase junction with v phase and η is the width of the interface.

The phase-field equation can be derived from the variation of the free energy functional, with the aim of minimizing the total free energy F

$$\frac{\partial\phi_\alpha}{\partial t} = -\sum_{\beta\neq\alpha}^{v} M_{\alpha\beta}\left(\frac{\delta F}{\delta\phi_\alpha} - \frac{\delta F}{\delta\phi_\beta}\right) \tag{5}$$

where $M_{\alpha\beta}$ is the anisotropic interface mobility between α and β phases. The multiphase problem can be decomposed into a sum of dual-phase transitions as follows:

$$\begin{aligned} \frac{\partial\phi_\alpha}{\partial t} = \sum_{\beta\neq\alpha}^{v}\tilde{M}_{\alpha\beta}\Bigg[&\frac{\sigma_{\alpha\beta}}{v}\left(\frac{1}{2}\left(\nabla^2\phi_\alpha - \nabla^2\phi_\beta\right) + \frac{\pi^2}{2\eta^2}\left(\phi_\alpha - \phi_\beta\right)\right) \\ &+ \sum_{\alpha\neq\beta\neq\gamma} J_{\alpha\beta\gamma} + \frac{\pi}{\eta}\sqrt{\phi_\alpha\phi_\beta}\Delta G_{\alpha\beta}\Bigg] \end{aligned} \tag{6}$$

where $J_{\alpha\beta\gamma} = \frac{1}{2}\left(\sigma_{\beta\gamma} - \sigma_{\alpha\gamma}\right)\left(\frac{\pi^2}{\eta^2}\phi_\gamma + \nabla^2\phi_\gamma\right)$ and $\Delta G_{\alpha\beta}$ is the thermodynamic driving force which is related to local temperature T and composition $\vec{c}$.

$$\Delta G_{\alpha\beta} = \frac{1}{V_m}\left(g_\beta - g_\alpha - \sum_{i=1}^{n-1}\tilde{\mu}^i\left(c_\beta^i - c_\alpha^i\right)\right) \tag{7}$$

The g_α and g_β are the molar Gibbs energy of α and β phases, and the Lagrange multiplier $\tilde{\mu}^i = \mu^i - \mu^n$ is the diffusion potential of the ith component, with the μ^i and μ^n being the chemical potential of the ith component and the solvent. And by multiplying molar volume V_m, the molar free energy can be transferred to volume free energy.

In the multiphase-field model, the extra freedom of separate phase compositions $\{\vec{c}_\alpha\}$ is fixed by quasi-equilibrium condition [19]. In this condition, the diffusion process is assumed to be much faster than the phase transformation process, and equal diffusion potential is stressed over the interface [17, 19].

$$\tilde{\mu}^i = \frac{dg_\alpha}{dc_\alpha^i} = \frac{dg_\beta}{dc_\beta^i} = \cdots = \frac{dg_v}{dc_v^i} \tag{8}$$

Together the with the mass constraint $\vec{c} = \sum_{\alpha=1}^{v}\phi_\alpha\vec{c}_\alpha$, the Newton's method can be used to solve these nonlinear equations. However, frequent access to thermodynamic databases and the Newton iteration process for all interface cells is time intensive. The extrapolation method [19, 22], which uses the Taylor's expansion, has provided a feasible way to solve the quasi-equilibrium condition with acceptable computational efficiency, and it is adopted in this work. The expression for the extrapolated thermodynamic driving force can be written as

$$\begin{aligned} \Delta G_{\alpha\beta}^{\text{Ext}} = &\sum_{i=1}^{n-1}\left(\frac{\partial\Delta G_{\alpha\beta}}{\partial c_\alpha^i}\right)\left(c_\alpha^{i,\text{Ext}} - c_\alpha^{i,\text{eq}}\right) \\ &+ \left(\frac{\partial\Delta G_{\alpha\beta}}{\partial T}\right)\left(T - T^{\text{eq}}\right) \end{aligned} \tag{9}$$

where $c_\alpha^{i,\mathrm{eq}}$ is the equilibrium concentration of ith component in α phase at reference temperature T^{eq}. In quasi-equilibrium condition, the phase compositions are not independent variables, and their relationship can be expressed by multibinary approximation [19, 22] using the coefficient $K_{\alpha\beta}^{ii} = \frac{\partial c_\alpha^i}{\partial c_\beta^i} = \frac{\partial \Delta G_{\alpha\beta}/\partial c_\beta^i}{\partial \Delta G_{\alpha\beta}/\partial c_\alpha^i}$. And the full derivation of the solution of local phase composition $\{\vec{c}_\alpha^{\mathrm{Ext}}\}$ under quasi-equilibrium constraint can be found in Ref. [19].

For dual interface, the mobility of the solid and liquid interface follows the thin interface limit [26, 27], and can be written as

$$\tilde{M}_{sl} = M_{sl}\frac{8\eta}{\pi^2} = \frac{16}{15a_2\eta}\frac{V_m}{RT}\sum_{i=1}^{n-1}\frac{D_l^i}{c_l^{i,\mathrm{eq}}\left(1-k_{sl}^i\right)^2} \tag{10}$$

where $a_2 = 0.6276$, T is the temperature, R is the gas constant, D_l^i is the diffusion coefficient of ith component in the liquid and $k_{sl}^i = c_s^{i,\mathrm{eq}}/c_l^{i,\mathrm{eq}}$ is the equilibrium partition coefficient, with $c_s^{i,\mathrm{eq}}$ and $c_l^{i,\mathrm{eq}}$ being the equilibrium concentration in solid and liquid phases.

To perform quantitative phase-field simulations, the anti-trapping current term is added into the solute transfer equation to eliminate anomalous interface effects [26–28]. In multicomponent superalloy system, if only liquid and solid (FCC) phases are considered, the time evolution equation of the concentration field can be expressed as

$$\frac{\partial c^i}{\partial t} = \nabla\left[\sum_{\alpha=l,s}\sum_{j=1}^{n-1} D_\alpha^{ij}\phi_\alpha\nabla c_\alpha^j + \frac{\eta}{\pi}\left(c_l^i - c_s^i\right)\sqrt{\phi_s\phi_l}\frac{\partial\phi_s}{\partial t}\frac{\nabla\phi_s}{|\nabla\phi_s|}\right] \tag{11}$$

where D_α^{ij} is the diffusion coefficient of component i and j in α phase.

Implementation

PF Eqs. (6) and (11) are solved in two dimensions on uniform finite difference grids using an explicit Euler time scheme. A high-precision nine-point stencil Laplacian operator is used in solving phase-field equation, and a standard five-point stencil Laplacian operator is used in solving solute diffusion equation. To reduce the amount of calculations, Eq. (6) and the anti-trapping current term in Eq. (11) are only computed near the solid–liquid interface where $|\nabla\phi|^2 > 1\times10^{-10}$. In addition, no thermal noise is added into the phase-field equation.

In directional solidification, the primary dendrite array needs quite a long time to reach a steady state [25, 29]. Therefore, to reduce the simulation cost, the moving-frame algorithm [24, 30] is used. At initial time, the dendrites at the bottom of the computational domain grow upwards naturally. When the maximum dendrite height reaches a critical value $H_{\max}$, the moving-frame algorithm works, and all the dendrite arms are kept under $H_{\max}$. For each lattice advance, the values of lattice points, including phase-field variables $\{\phi_\alpha(\vec{x},t)\}$ and solute concentrations $\{\vec{c}_\alpha(\vec{x},t)\}$, are transfer to the lower lattice points along y-direction. And the lattice points at the top of computational domain are set with the initial values as in the liquid.

GPU-based parallel computation

The large-scale phase-field simulation of multicomponent nickel-based superalloy dendrite growth in directional solidification condition requires large computational cost. To accelerate the computation, we adopt a previously developed GPU-based parallel computing scheme [23], and this algorithm has been optimized by using the GPU shared memory as user managed cache. All the simulations were performed on a GPU server with 8 NVIDIA GTX1080Ti GPUs, and each simulation case was processed by one GPU. The relative large computational domain size and long simulation time are chosen to ensure reliable results on the steady primary dendritic spacing. As for the simulation time, the shortest simulation with the computational domain of $4096 \times 758\ \mu m^2$ over 2×10^7 steps lasts about 7 h, and the longest simulation with the domain size of $8192 \times 1536\ \mu m^2$ over 1.5×10^7 steps lasts about 80 h. Compared with the performance on an Intel Xeon CPU E5-2680 v4 at 2.4 Ghz, the GPU-based computing scheme generally achieves more than 200 times speed-up ratio.

Alloy and simulation conditions

Owing to its extensive research and usage, a second-generation superalloy CMSX-4 [31–33] is investigated in this work, and the alloy chemical compositions [33] are listed in Table 1. To reduce the computation time, the alloy components in CMSX-4 with less than

Table 1 Chemical compositions of the investigated alloys [33]

Alloy	Al	Co	Cr	Hf	Mo	Re	Ta	Ti	W	Ni
CMSX-4 (wt%)	5.65	9.6	6.4	0.1	0.61	2.9	6.5	1.01	6.4	Bal.
CMSX-4 (at.%)	12.72	9.90	7.48	0.03	0.39	0.95	2.18	1.28	2.11	Bal.
Model alloy (at.%)	12.72	9.90	7.48	–	–	0.95	2.18	1.28	2.11	Bal.

0.5 at.% are excluded, and the model alloy is used in all the simulations.

The equilibrium parameters used in multiphase-field simulations are calculated by Pandat and PanEngine software using PanNi database. All the parameters are updated with a temperature interval of 0.2 K [22] during simulations to ensure accuracy. The equilibrium parameters of the model alloy at $T^* = 1621.2$ K are shown in Table 2 as an example. And the equilibrium concentrations of Al, Co, Cr, Re, Ta versus temperature are shown in Fig. 1 during solidification interval of 1656–1573 K. The concentration data are calculated using shell mode in Pandat software, and the derivatives of chemical driving force with respect to phase concentrations are calculated using PanEngine software.

To investigate the superalloy primary dendrite spacing selection in directional solidification, the effects of temperature gradient G, pulling velocity V_p and the grain inclination angle θ are considered. Initially, the computational domain is set to be rectangle with a temperature gradient along y-direction. And the temperature is assumed to follow the frozen temperature approximation $T = T_0 + G(y - V_p t)$, where T_0 is the reference temperature at $y = 0$ and t is the time. Because the initial setting of the seed space has a history effect [29, 30] on the final primary dendrite spacing, a continues seed bed with random noise on the surface was adopted to imitate the natural incubation of dendrite arms, which is shown as case 1 and case 2 in Fig. 2. The seeds in the seed bed have the same crystal orientation. In addition, several types of random noises were tested to make sure the initial condition does not influence the final steady primary dendritic spacing. The misoriented continuous seed bed was set to study the effect grain inclination angle with respect to the heat-flow direction, which is shown as case 2 in Fig. 2. During each simulation, the periodic boundary condition was applied to the y-boundaries, and the adiabatic boundary condition was applied to the x-direction.

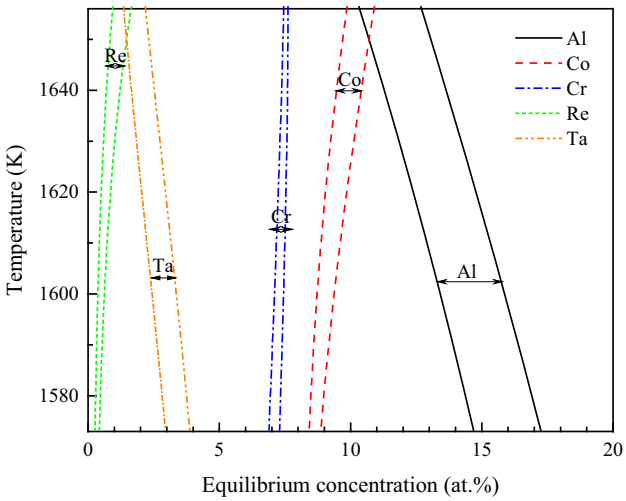

Figure 1 The equilibrium concentration of component Al, Co, Cr, Re, Ta in liquid and FCC phases in the solidification interval of 1656–1573 K (the concentration of Ti and W is not shown in the figure).

Table 2 Equilibrium parameters of the model alloy at $T^* = 1621.2$ K

Parameters	Al	Co	Cr	Re	Ta	Ti	W
$c_l^{eq}(T^*)$ at.%	14.7201	9.0653	7.2529	0.5096	2.9281	1.6564	1.6430
$c_s^{eq}(T^*)$ at.%	12.3332	9.8820	7.5414	0.8691	2.0212	1.1923	2.1494
$D_l(T^*) \times 10^9$ m^2 s^{-1}	2.9922	1.0123	1.1259	0.9869	1.7381	1.4159	1.0639
$D_s(T^*) \times 10^{12}$ m^2 s^{-1}	1.9635	0.4945	0.3504	0.0021	0.1687	0.2848	0.0076
$\partial\Delta G_{sl}/\partial c_l^{eq}$ J mol^{-1} at	− 7743.25	− 1305.15	− 4646.75	42109.46	− 11556.75	− 11453.10	− 1880.95
$\partial\Delta G_{sl}/\partial c_s^{eq}$ J mol^{-1} at	− 8129.24	− 1251.97	− 4685.67	21830.01	− 12378.07	− 11215.61	− 3483.90
K_{sl}^{eq} (multibinary)	0.9525	1.0425	0.9917	1.9290	0.9336	1.0212	0.5399

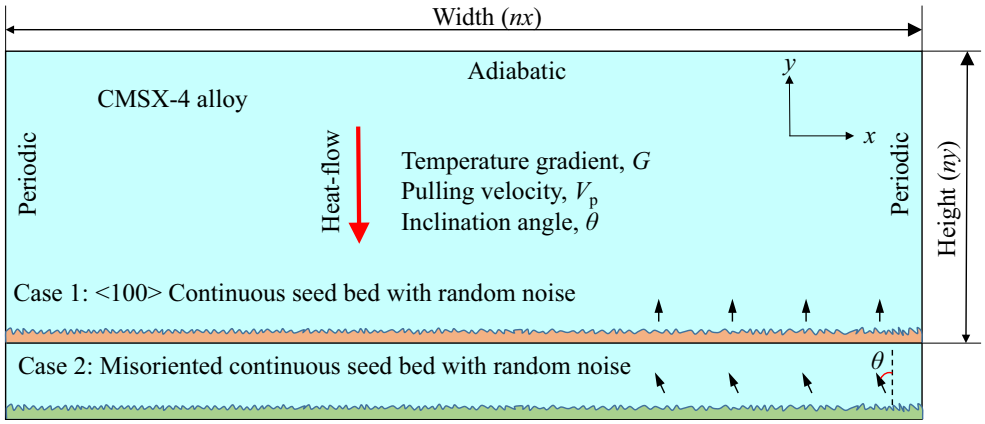

Figure 2 Schematic of the setup of the computational domain.

Table 3 Simulation parameters in directional solidification of model alloy

Parameters	Unit	Values
Initial temperature, T_0	K	− 4.0
Temperature gradient, G	K mm^{-1}	2, 5, 10, 20, 50, 100, 200
Pulling velocity, V_p	μm s^{-1}	10, 20, 50, 100, 200, 500
Inclination angle, θ	°	0, 5, 10, 15, 20, 25, 30, 35, 40
Grid size, Δx	μm	1.0
Interface width, η	μm	4.0
Kinetic anisotropy coefficient, δ_k	–	0.05 [34]
Static anisotropy coefficient, δ_s 0.02	–	0.02 [34]
Maximum height, H_{max}	–	0.70
Molar volume, V_m	m^3 mol^{-1}	7.8 × 10^{-6}
Interface energy, $\sigma_{Liquid/FCC}$	J m^{-2}	0.161 [35]
Time step, Δt	s	7.0 × 10^{-5}

Table 4 The solidification conditions in the orthogonal design of simulations (full range means all the corresponding values listed in Table 3 are used)

Case	Temperature gradient, G	Pulling velocity, V_p	Inclination angle, θ	Domain size
1	2, 5 K mm^{-1}	Full range	0°	8192 × 1536 μm^2
1	10, 20, 50, 100 K mm^{-1}	Full range	0°	4096 × 1024 μm^2
1	200 K mm^{-1}	Full range	0°	4096 × 768 μm^2
2	10, 20, 50 K mm^{-1}	100 μm s^{-1}	Full range	4096 × 1024 μm^2

The moving-frame algorithm was triggered when the maximum dendrite tip height reaches 0.7 × ny. The other parameters used in multiphase-field simulations are listed in Table 3.

In case 1, an orthogonal experimental design was used, the pulling velocities were set to V_p = 10, 20, 50, 100, 200 and 500 μm s^{-1}, and the temperature gradients were set to G = 2, 5, 10, 20, 50, 100 and 200 K mm^{-1}, as listed in Table 4. The simulation conditions have covered the typical processing conditions of high-rate solidification technique (HRS, V_p = 10–100 μm s^{-1}, G = 2–5 K mm^{-1}), liquid metal cooling (LMC, V_p = 50–400 μm s^{-1}, G = 8–20 K mm^{-1}) and high-gradient directional solidification technique by zone melting liquid metal cooling (ZMLMC, G = 10–100 K mm^{-1}) [2, 3, 36]. The computational domain was set to $nx \times ny$ = 4096 × 768 μm^2 for G = 200 K mm^{-1}, $nx \times ny$ = 4096 × 1024 μm^2 for G = 200, 100, 50, 20 and 10 K mm^{-1}, and $nx \times ny$ = 8192 × 1536 μm^2 for G = 5 and 2 K mm^{-1}. And the simulation times were set to 2–15 × 10^6 steps to ensure a minimum pulling distance of 10 mm under different pulling velocities. In case 2, the pulling velocity V_p was set to be fixed at 100 μm s^{-1}, the temperature gradient G was set

to 10, 20 and 50 K mm^{-1}, and the grain inclination angle varied from 0° to 40° with a 5° interval as listed in Table 4.

Results and discussion

Interface morphologies and microsegregation

In superalloy directional solidification, the pulling velocity along with the temperature gradient has a great impact on the morphology of the solidification front [3–9] and the microsegregation pattern [31, 32]. This part gives an overview of the observed microstructure under pulling velocities V_p = 0.5–100 μm s^{-1} and temperature gradients G = 20–100 K mm^{-1} as Liu [3] did in experiments.

Figure 3 shows the solid–liquid interface morphology under different simulation conditions. The solidification front exhibits a planar interface at V_p = 0.5 μm s^{-1} and G = 20 K mm^{-1}, as shown in Fig. 3a. As the pulling velocity increases from 0.5 to 100 μm s^{-1}, the interface gradually evolves in the sequence of planar, coarse dendrite (Fig. 3b) and fine dendrite (Fig. 3c, d). At high-temperature gradients $G \geq 50$ K mm^{-1}, the growth of side branches is suppressed, and fine dendrite–cellular pattern and superfine cellular structure are found in Fig. 3e, f, respectively.

The multiphase-field model takes account of the multicomponent solute transfer in the solid and liquid, as well as the anti-trapping current. When coupling with thermodynamic database, it is capable of investigating the microsegregation pattern in superalloy directional solidification. The segregation pattern (Fig. 4a) under solidification condition of V_p = 50 μm s^{-1} and G = 5 K mm^{-1} is taken as an example, the processing condition of which is close to the conventional Bridgman high-rate solidification technique (HRS). Figure 4b–f shows the solute distribution of components Al, Co, Cr, Re, Ta, Ti and W. The components Co, Cr, Re and W segregate to the solidified dendrite arms, while Al, Ta, Ti segregate to the remaining melt. The segregation tendency is in consistent with experiment results of CMSX-4 [31].

To quantitatively investigate the segregation behavior of each alloy component, the concentration profile at the root of the dendrite arm in Fig. 4a is extracted and plotted in Fig. 5a. The partition coefficients $\bar{k}^i = \bar{c}_s^i/\bar{c}_l^i$ of all components are calculated by using the average concentration in the solid $\bar{c}_s^i$ and liquid $\bar{c}_l^i$. Then, the calculated average partition coefficients $\bar{k}^i$ along with the results based on EPMA analysis of CMSX-4 samples produced under cooling rate of 0.25 K s^{-1} [31] are presented in Fig. 5b. The simulation results of the partition coefficient agree well with the experiment in terms of Al, Co, Re, Ta, Ti and W, while the result of Cr exhibits a major difference with the experiment. It is true that Cr segregates moderately during γ solidification ($\bar{k}^{Cr}$ close to unity) [37], but the solubility of Cr is much lower in γ' phase, which results in a pile up between the γ dendrite and γ/γ' eutectic. Since our multiphase-field simulation did not take account the growth of γ'

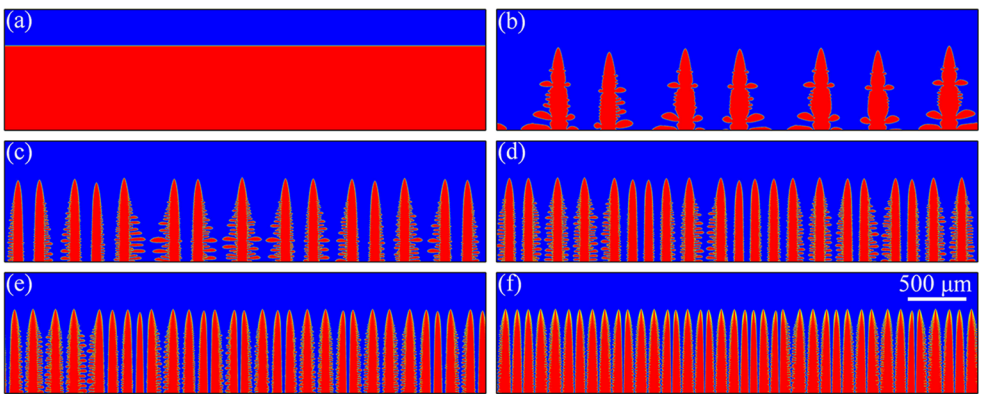

Figure 3 Interface morphologies at solidification front under different processing conditions: **a** plane interface under V_p = 0.5 μm s^{-1} and G = 20 K mm^{-1}, **b** coarse dendrite under V_p = 5 μm s^{-1} and G = 20 K mm^{-1}, **c** fine dendrite under V_p = 50 μm s^{-1} and G = 20 K mm^{-1}, **d** fine dendrite under V_p = 100 μm s^{-1} and G = 20 K mm^{-1}, **e** fine dendrite-cellular under V_p = 100 μm s^{-1}, G = 50 K mm^{-1}, **f** superfine cellular under V_p = 100 μm s^{-1} and G = 100 K mm^{-1}.

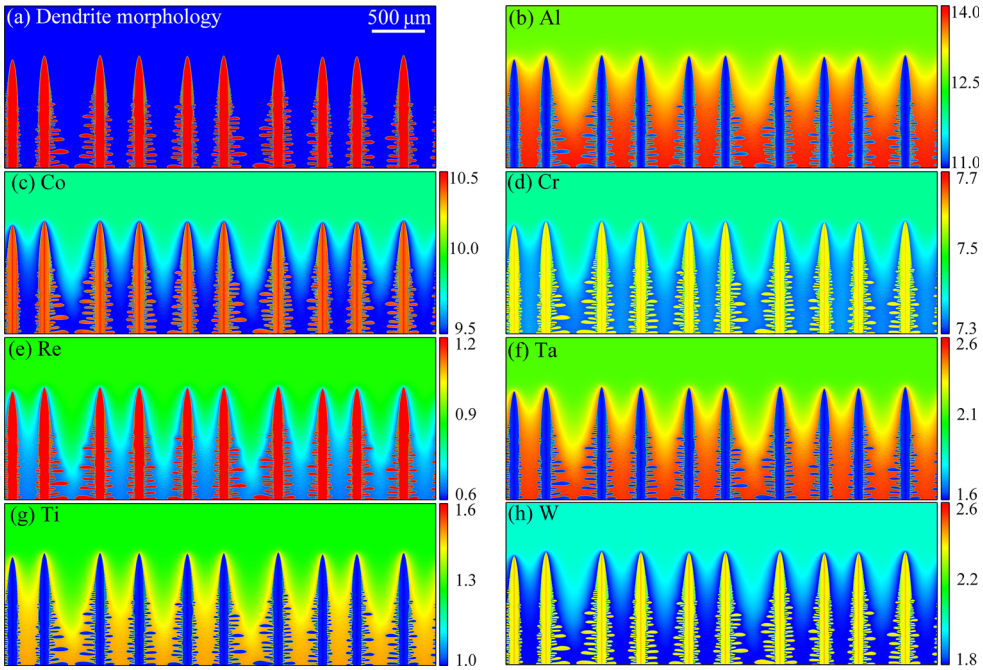

Figure 4 **a** Dendrite morphology and **b**–**h** solute distribution of component Al, Co, Cr, Re, Ta, Ti, W under steady state at puling velocity of 50 μm s^{-1} and temperature gradient of 5 K mm^{-1}.

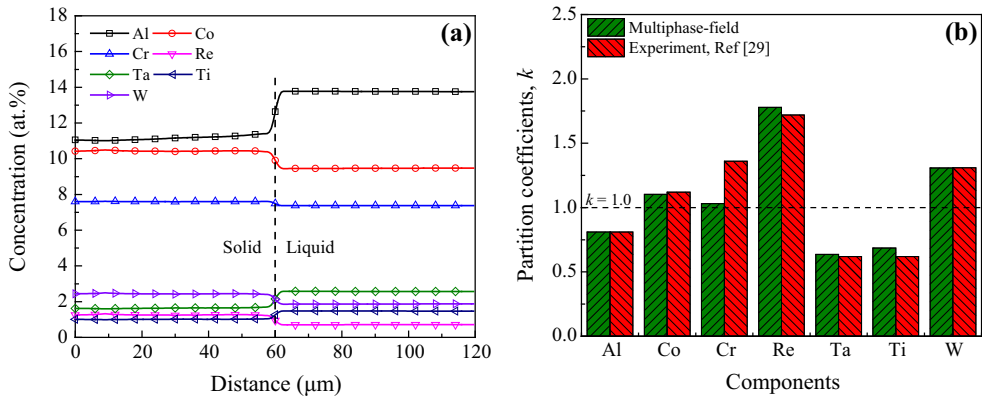

Figure 5 **a** The concentration profile at the root of the dendrite arm at puling velocity of 50 μm s^{-1} and temperature gradient of 5 K mm^{-1}, which presents a cooling rate of 0.25 K s^{-1}. **b** The interface partition coefficient of all the components calculated from multiphase-field simulation and obtained from experimental results in Ref. [31] using F–G sort method. The CMSX-4 samples are produced under cooling rate of 0.25 K s^{-1}.

phase, the segregation pattern of Cr cannot be correctly predicted.

Effect of temperature gradient and pulling velocity

In this part, the effects of temperature gradient G and pulling velocity V_p on the final primary arm spacing are systematically investigated. In classical theories [12, 13], the primary dendrite spacing Λ can be estimated with analytical function as shown in Eq. (1). As mentioned above, the initial condition of the artificially settled seeds has a history effect on the final dendrite arm spacing. Therefore, we employ a continuous seed bed with random noise on the surface to imitate the natural development of dendrite arm. Figure 6 shows a typical growth process of the directional solidified model superalloy. This process includes initial planar instability, adjustment of primary dendrite arm spacing through elimination and steady-state dendrite growth. In the orthogonal test, the solidification conditions in all the simulations are listed as case 1 in Table 4.

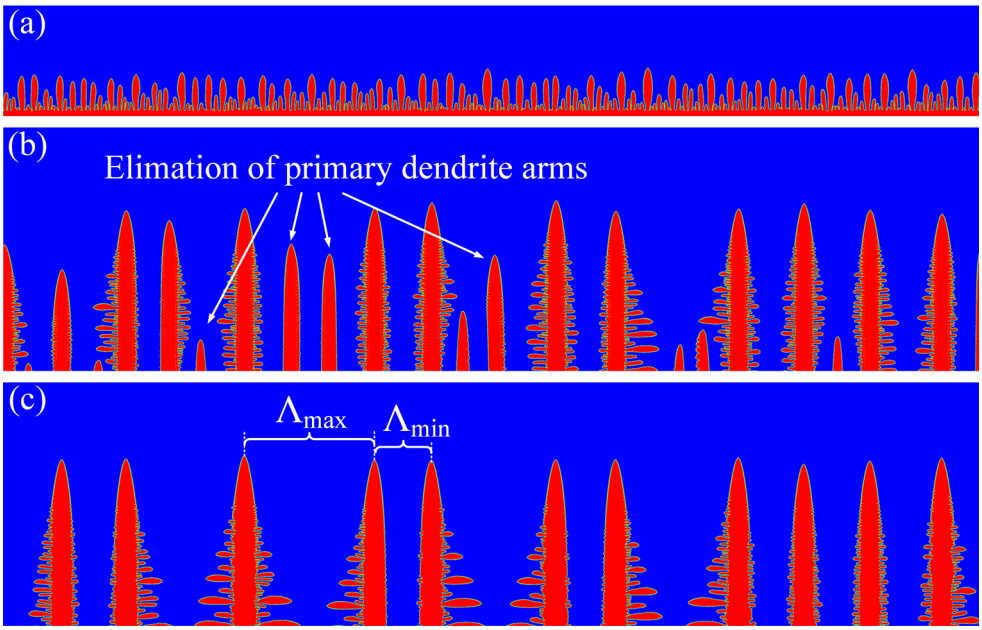

Figure 6 A typical growth process of the directional solidified model superalloy: **a** small bubs from a continuous seed bed, solidification time = 28 s, **b** elimination of primary dendrite arms and adjustment of dendrite arm spacing, solidification time = 56 s, **c** primary dendrite arm array under steady state, solidification time = 420 s.

Figure 7 shows the final dendrite morphology under all solidification conditions, and the primary dendrite arms exhibit a prominent morphology change. In general, monotonously increasing temperature gradient and pulling velocity can both decrease the primary dendrite spacing. The number of primary arms under temperature gradients of 5 and 2 K mm^{-1} is more than that in the case of 10 K mm^{-1}, because the computational domain is larger in the former. When under large temperature gradients, the secondary dendrite arm is suppressed even if the pulling velocity is small. This phenomenon is similar to Tien's findings [38].

Because the sizes of the computational domain are different, the number of primary dendrite arms in x-direction is normalized by a width of 4 mm during simulations, and the results are shown in Fig. 8. Here, the tips of primary dendrite arms which grow higher than $0.5 \times ny$ were taken into account. The number of dendrite arms in all the simulations has undergone three typical stages: an explosive rise and sharply fall process, a gradual decline process and an unchanged steady state. A phony increase in the number of dendrite arms under temperature gradients $G = 2$ and 5 K can be observed during the second stage. This is because the dendrite arms under $0.5 \times ny$ were not taken into account, and the primary dendrite arms under low-temperature gradient need a quite long time to adjust their positions through competitive growth. In fact, the number of dendrite arms is gradually decreasing. The number of primary dendrite arms generally decreases with temperature gradient in all the cases. In order to quantitatively investigate the effect of temperature gradient G and the pulling velocity V_p, the primary dendrite arm spacing under steady state is fitted using the analytical model in Eq. (1).

The fitting results are shown in Figs. 9 and 10. The graphs are plotted with two sets of axis: one for the temperature gradient G or pulling velocity V_p on a logarithmic scale and one for primary dendrite arm spacing (PDAS) on a linear scale. The points at each solidification condition represent the maximum, average and minimum primary dendrite spacing under final steady state obtained from three repeated simulations. The fitting results of the average value of PDAS (Λ_{ave}) are shown as curves, along with the formulas. The range [Λ_{min}, Λ_{max}] of PDAS is also shown in the figures. In contrast to classical theory where $b = 0.5$ and $c = 0.25$, the value of b and c is generally changing under different cooling conditions. The value of b varies slightly from 0.34 to 0.42 in our measurements, and b is near 0.38 in most cases, while the value of c increases monotonously from 0.27 to 0.56 with decreasing temperature gradient G. The details of each b and c are shown in Table 5, and the goodness of the fitting results is evaluated by adjusted coefficient of determination R^2, which is also provided in Table 5.

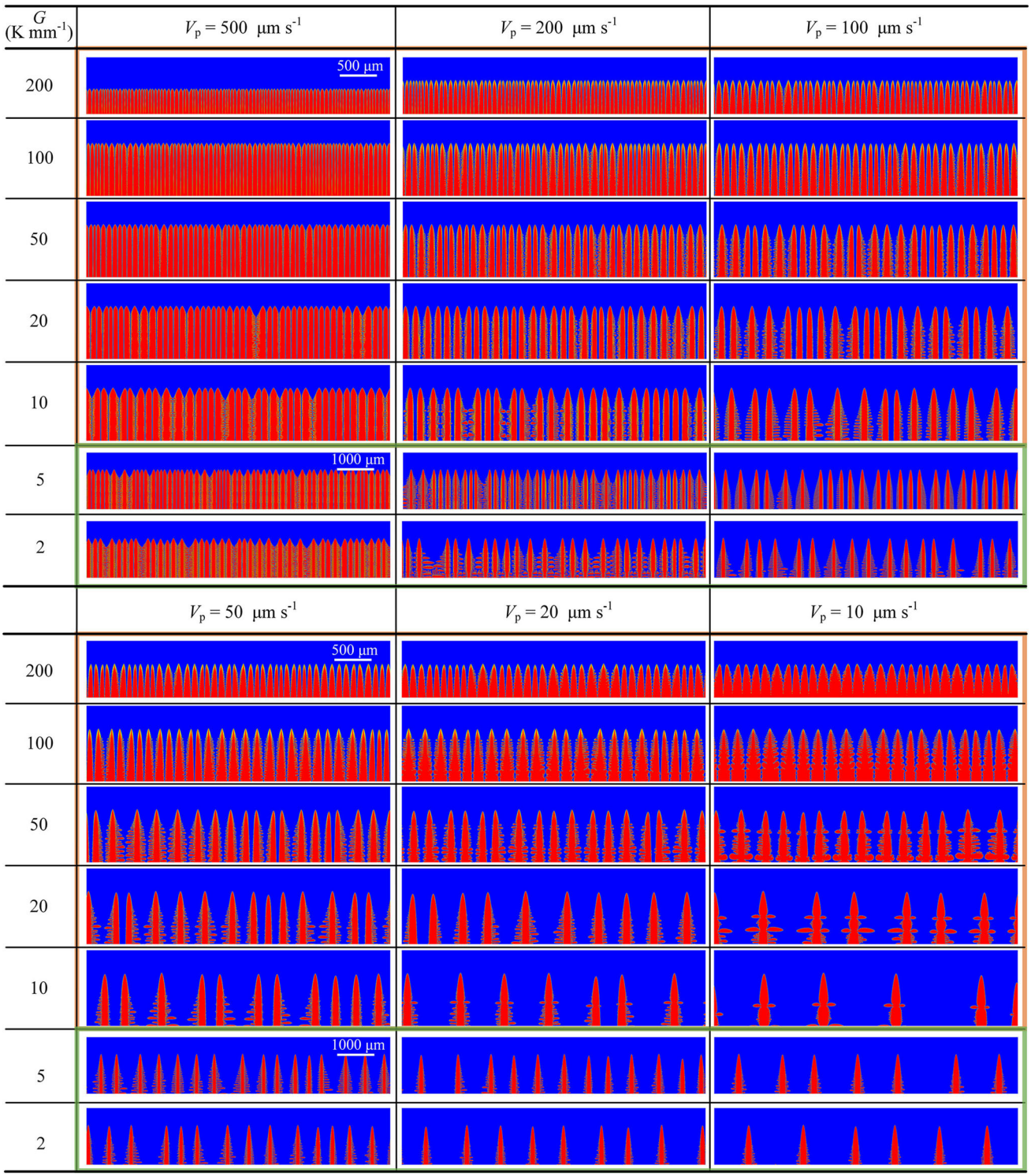

Figure 7 The final dendrite morphologies under different solidification conditions of pulling velocity V_p = 500, 200, 100, 50, 20 and 10 μm s^{-1} and temperature gradient G = 200, 100, 50, 20 and 10 K mm^{-1}.

In 2D simulations, the solute at the dendrite tip cannot diffuse so efficient as in 3D; therefore, the predicted average primary dendrite spacing in 3D should also be smaller than in 2D. To compare the Λ_{ave} calculated from 2D multiphase-field simulations with the experimental data, the Λ_{ave} are modified by

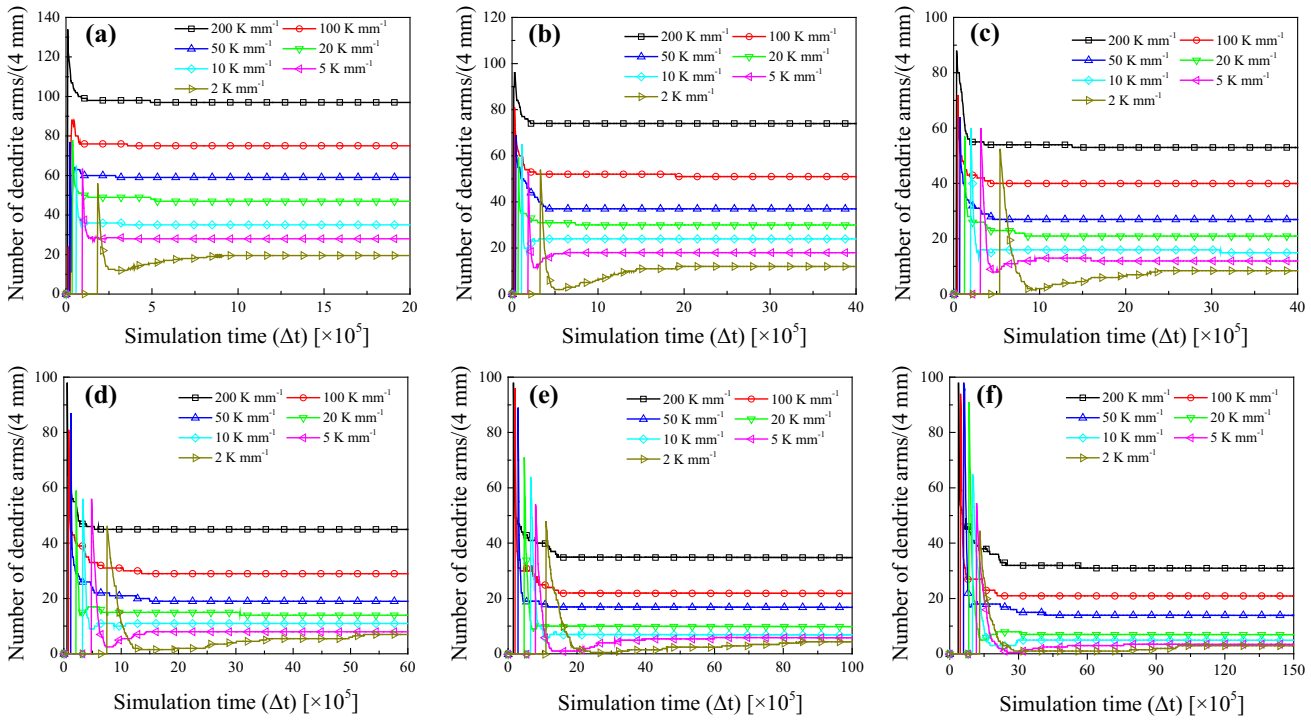

Figure 8 Number of dendrite arms per 4 mm in *x*-direction under pulling velocity range of: **a**–**f** V_p = 500, 200, 100, 50, 20 and 10 μm s^{-1}, with the temperature gradient *G* being 200–2 K mm^{-1}.

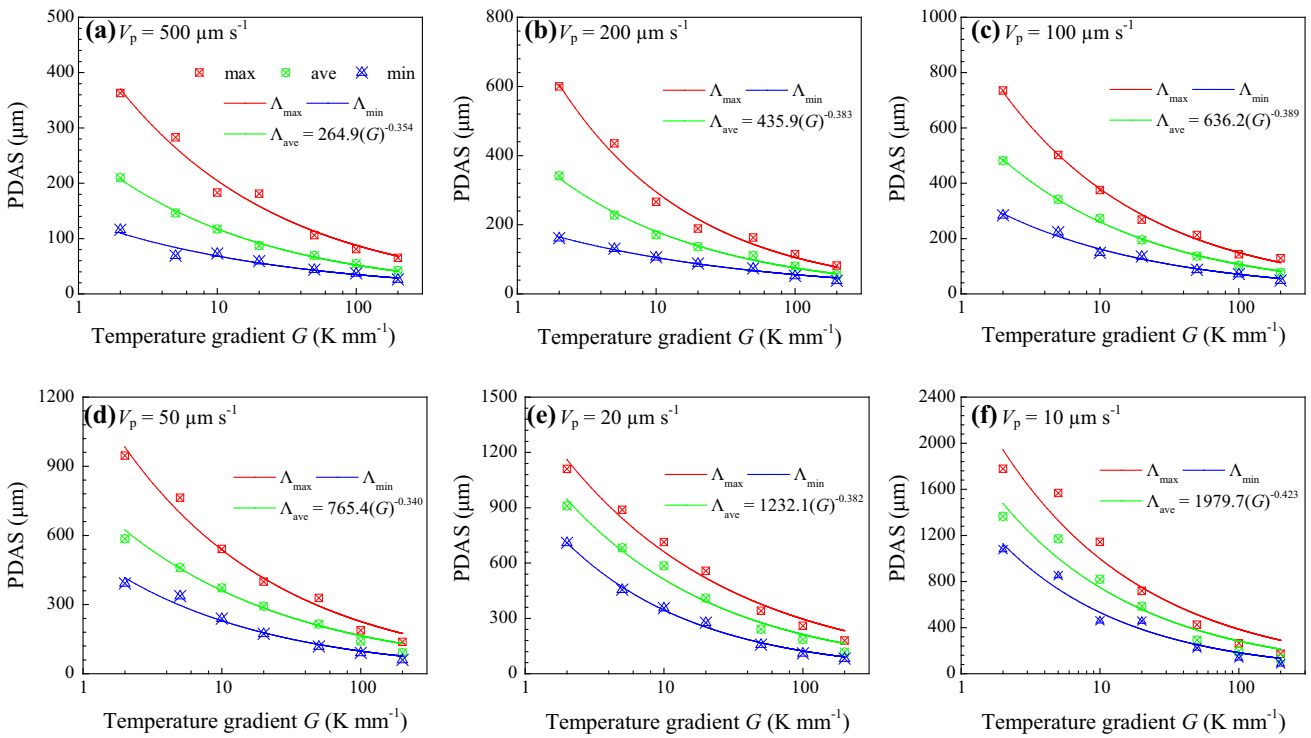

Figure 9 The maximum, average and minimum primary dendrite arm spacing (PDAS) as a function of temperature gradient *G* (2–200 K mm^{-1}) under different pulling velocities **a**–**f** V_p = 500, 200, 100, 50, 20, 10 μm s^{-1}. The fitting curves are presented along with the formula of Λ_{ave}.

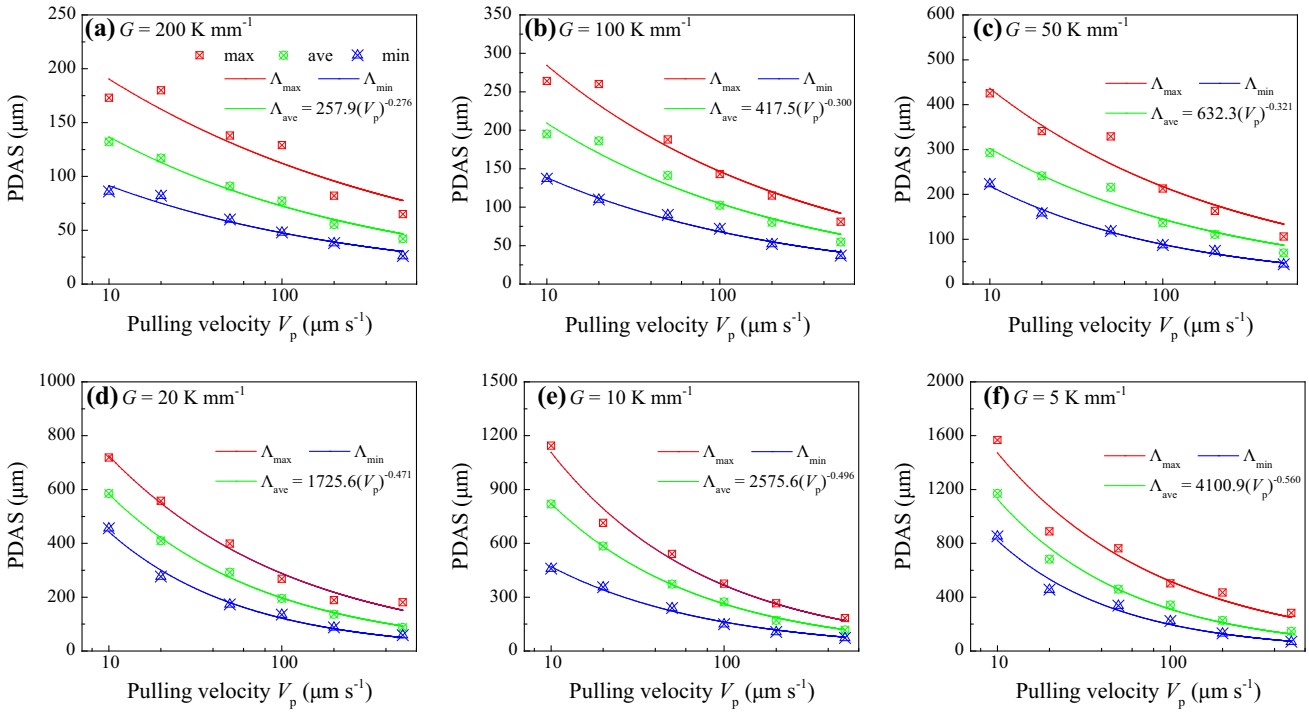

Figure 10 The maximum, average and minimum primary dendrite arm spacing (PDAS) as a function of pulling velocity V_p (500–10 μm s^{-1}) under different temperature gradients **a**–**f** G = 200, 100, 50, 20, 10, 5 K mm^{-1}. The fitting curves are presented along with the formula of Λ_{ave}.

Table 5 Fitting results of variables b and c under different cooling conditions

V_p (μm s^{-1})	500	200	100	50	20	10
b	0.354	0.383	0.389	0.340	0.382	0.423
Adjusted R^2	0.996	0.991	0.998	0.979	0.973	0.943
$\bar{\Lambda}_{max}/\bar{\Lambda}_{min}$	2.84	2.61	2.35	2.34	2.04	1.95
G (K mm^{-1})	200	100	50	20	10	5
c	0.276	0.300	0.321	0.471	0.496	0.560
Adjusted R^2	0.977	0.943	0.942	0.996	0.998	0.982
$\bar{\Lambda}_{max}/\bar{\Lambda}_{min}$	2.31	2.13	2.31	2.18	2.38	2.62

multiplying a factor of $\sqrt{2}/2$ [29]. The final results are shown in Fig. 11. The experiments in Ref. [5] use second-generation superalloys PWA1484 and RenéN5 with conventional Bridgman HRS technique, and the experiments in Ref. [3] use a first-generation CMSX-2 superalloy with ZMLMC technique, which can provide a very high temperature gradient of 100 K mm^{-1}. The simulation results have a good approximation for Λ_{ave} when under high pulling velocities, while the predicted Λ_{ave} under lower pulling velocities exhibit higher values than that in experiments. Moreover, the coarse cellular structure [3, 38] under low pulling velocity of 10 μm s^{-1} is not reproduced by multiphase-field simulation. The deviation of PDAS the under low pulling velocities could be ascribed to the convection in the liquid [39–41], which is not considered in the current multiphase-field model. The thermal and solutal gradients, combined with the effect of gravity, can lead to significant natural convection in the liquid alloy and thus change the morphology of the solid front.

Effect of grain inclination angle

Despite a series of controlling techniques [42, 43], a fraction of single-crystal turbine blades are produced with their <001> crystal orientation deviate from the withdraw (heat-flow) direction up to 15° [44–46]. The understanding of primary dendrite arm spacing under misalign withdraw direction can be vital to industrial production. Therefore, in this part, the effect of grain inclination angle on the final PDAS was investigated. All the solidification conditions are listed as case 2 in Table 4.

Figure 12 shows the final dendrite morphology with grain inclination angle of 0°, 10°, 20°, 30° and 40°

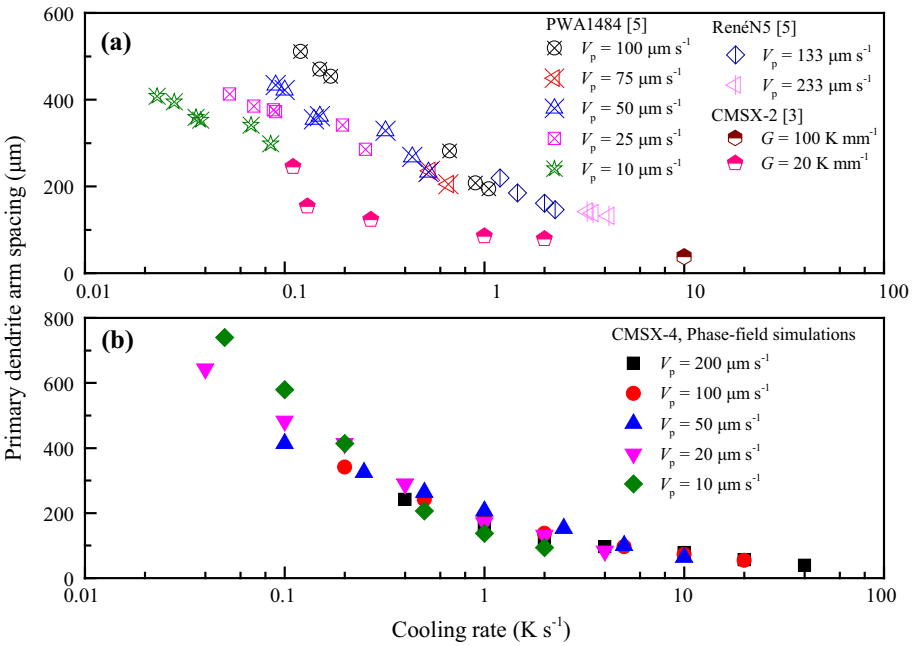

Figure 11 **a** Average primary dendrite arm spacing obtained from experiments in Refs. [3, 5, 6], **b** the modified average primary dendrite arm spacing $\tilde{\lambda}_{ave}$ calculated from multiphase-field simulations.

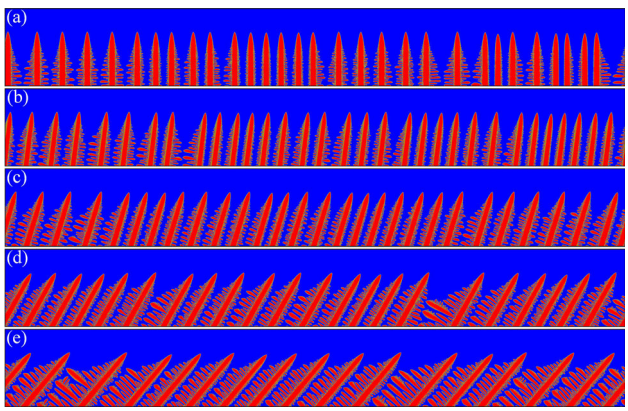

Figure 12 Final dendrite morphology under with different grain orientations **a**–**e** $\theta = 0°$, 10°, 20°, 30° and 40°. The cooling condition is V_p = 100 μm s^{-1} and G = 10 K mm^{-1}.

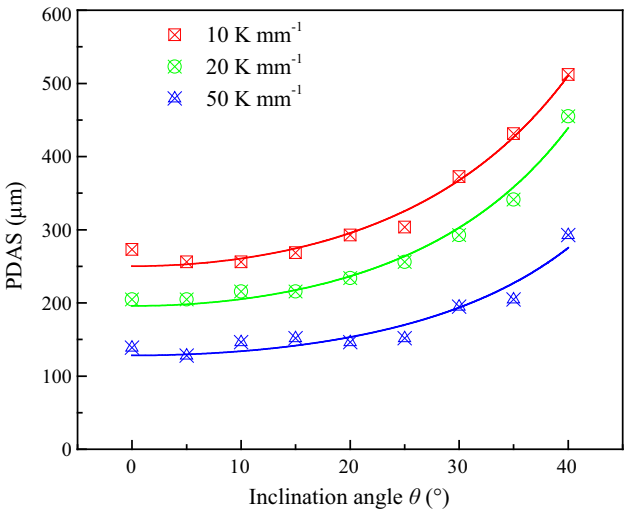

Figure 13 Variation of primary dendrite arm spacing with inclination angle θ under temperature gradients of 10, 20, 50 K mm^{-1} and pulling velocity of 100 μm s^{-1}.

under temperature gradient of G = 10 K mm^{-1}. It can be seen that, with the increase in inclination angle, the dendrites have more developed secondary arms in the side toward which it drifts. The fully developed secondary arms can block the undeveloped primary dendrite arms and thus increase the PDAS. The calculated average PDAS with different crystal orientations is shown in Fig. 13, and the discrete points are fitted using the power function in Eq. (2). An abnormal decrease in PDAS with grain inclination angle θ was observed when $\theta < 10°$, and this is not consistent with classical theory that PDAS always increases with inclination angle. Moreover, the PDAS almost remains constant within inclination angle of 20° in the three temperature gradients. As long as the inclination angle exceeds 20°, the PDAS shows a significant rise and increases as a power function. The coefficients in Eq. (2) we estimated with our fitting results are d = 0.07 and e = 2.8.

Summary and conclusions

The primary dendrite arm spacing selection in a directional solidified superalloy CMSX-4 was studied using two-dimensional phase-field simulations. The alloy thermodynamic and kinetic data are obtained from Pandat software with PanNickel database, and extrapolation method was used to couple the thermodynamic data with multiphase-field model. With the help of a previously developed GPU parallel computing scheme, we are able to perform hundreds of large-scale phase-field simulations on a multi-GPU server. In the orthogonal simulations, a wide range of processing conditions including pulling velocities (V_p = 10, 20, 50, 100, 200, 500 μm s^{-1}) and temperature gradients (G = 2, 5, 10, 20, 50, 100, 200 K mm^{-1}) are applied to systematically study the primary dendrite spacing variation. The simulation results are analyzed using a classical analytical model $\Lambda \propto \Delta T_0^a V_p^{-b} G^{-c}\{1 + d[(\cos\theta)^{-e} - 1]\}$, and the coefficients b, c, d, e are determined by the fitting results. The main findings are listed as follows:

1. The multiphase-field model coupled with CALPHAD can be used to study the multicomponent superalloy microstructure evolution and segregation behavior, and the simulation results are quantitatively in consistent with experimental results.
2. In the phase-field simulations, the fitting results of primary dendritic spacing exhibit excellent goodness with the power law, the coefficient b is near 0.38 under different pulling velocities, while the coefficient c increases from 0.27 to 0.56 with increasing temperature gradient.
3. The primary dendrite spacing experienced a subtle decrease with increasing grain inclination angle θ when $\theta < 10°$. As θ exceeds 20°, the primary dendrite spacing increases significantly with increasing θ. The coefficients estimated from our fitting results are d = 0.07 and e = 2.8.

Acknowledgements

This research was funded by the National Key Research and Development Program of China (2017YFB0701503), National Science and Technology Major Project (No. 2017ZX04014001) and the National Natural Science Foundation of China (No. 51374137).

Compliance with ethical standards

Conflict of interest The authors declare that they have no conflict of interest.

References

[1] Versnyder FI, Shank M (1970) The development of columnar grain and single crystal high temperature materials through directional solidification. Mater Sci Eng 6:213

[2] Giamei AF, Tschinkel JG (1976) Liquid metal cooling: a new solidification technique. Metall Trans A 7:1427

[3] Liu L, Huang T, Zhang J, Fu H (2007) Microstructure and stress rupture properties of single crystal superalloy CMSX-2 under high thermal gradient directional solidification. Mater Lett 61:227

[4] Quested P, McLean M (1984) Solidification morphologies in directionally solidified superalloys. Mater Sci Eng 65:171

[5] Whitesell H, Li L, Overfelt R (2000) Influence of solidification variables on the dendrite arm spacings of Ni-based superalloys. Metall Mater Trans B 31:546

[6] Li LC (2002) Microstructural development and segregation effects in directionally solidified nickel-based superalloy PWA 1484. ProQuest Dissertations and Theses, Ph.D. thesis, Auburn University, pp 65–86

[7] Konter M, Thumann M (2001) Materials and manufacturing of advanced industrial gas turbine components. J Mater Process Technol 117:386

[8] Reed RC (2008) The superalloys: fundamentals and applications. Cambridge University Press, Cambridge

[9] Wagner A, Shollock BA, Mclean M (2004) Grain structure development in directional solidification of nickel-base superalloys. Mater Sci Eng A 374:270

[10] Dsouza N, Ardakani M, Wagner A, Shollock B, McLean M (2002) Morphological aspects of competitive grain growth during directional solidification of a nickel-base superalloy, CMSX4. J Mater Sci 37:481. https://doi.org/10.1023/A:1013753120867

[11] Liang Z, Xu Q, Li J, Li S, Zhang J, Liu B, Zhong Z (2002) Experimental research on the near net shape casting process of gamma titanium aluminide turbochargers. Rare Met Mater Eng 31:353

[12] Hunt J (1979) Solidification and casting of metals. In: Proceedings of conference, Sheffield, England, July 1977

[13] Kurz W, Fisher D (1981) Dendrite growth at the limit of stability: tip radius and spacing. Acta Metall 29:11

[14] Gandin CA, Eshelman M, Trivedi R (1996) Orientation dependence of primary dendrite spacing. Metall Mater Trans A 27:2727

[15] Schneider MC, Gu JP, Beckermann C, Boettinger WJ, Kattner UR (1997) Modeling of micro-and macrosegregation and freckle formation in single-crystal nickel-base superalloy directional solidification. Metall Mater Trans A 28:1517

[16] Karma A, Rappel W-J (1996) Phase-field method for computationally efficient modeling of solidification with arbitrary interface kinetics. Phys Rev E 53:R3017

[17] Kim SG, Kim WT, Suzuki T (1999) Phase-field model for binary alloys. Phys Rev E 60:7186

[18] Steinbach I, Pezzolla F (1999) A generalized field method for multiphase transformations using interface fields. Physica D 134:385

[19] Eiken J, Böttger B, Steinbach I (2006) Multiphase-field approach for multicomponent alloys with extrapolation scheme for numerical application. Phys Rev E 73:066122

[20] Tang J, Xue X (2009) Phase-field simulation of directional solidification of a binary alloy under different boundary heat flux conditions. J Mater Sci 44:745. https://doi.org/10.1007/s10853-008-3157-1

[21] Warnken N, Ma D, Drevermann A, Reed RC, Fries S, Steinbach I (2009) Phase-field modelling of as-cast microstructure evolution in nickel-based superalloys. Acta Mater 57:5862

[22] Böttger B, Eiken J, Apel M (2015) Multi-ternary extrapolation scheme for efficient coupling of thermodynamic data to a multi-phase-field model. Comput Mater Sci 108:283

[23] Yang C, Xu Q, Liu B (2017) GPU-accelerated three-dimensional phase-field simulation of dendrite growth in a nickel-based superalloy. Comput Mater Sci 136:133

[24] Takaki T, Ohno M, Shimokawabe T, Aoki T (2014) Two-dimensional phase-field simulations of dendrite competitive growth during the directional solidification of a binary alloy bicrystal. Acta Mater 81:272

[25] Takaki T, Sakane S, Ohno M, Shibuta Y, Shimokawabe T, Aoki T (2016) Primary arm array during directional solidification of a single-crystal binary alloy: large-scale phase-field study. Acta Mater 118:230

[26] Kim SG (2007) A phase-field model with antitrapping current for multicomponent alloys with arbitrary thermodynamic properties. Acta Mater 55:4391

[27] Carré A, Böttger B, Apel M (2013) Implementation of an antitrapping current for a multicomponent multiphase-field ansatz. J Cryst Growth 380:5

[28] Karma A (2001) Phase-field formulation for quantitative modeling of alloy solidification. Phys Rev Lett 87:115701

[29] Wang W, Lee PD, Mclean M (2003) A model of solidification microstructures in nickel-based superalloys: predicting primary dendrite spacing selection. Acta Mater 51:2971

[30] Diepers H-J, Ma D, Steinbach I (2002) History effects during the selection of primary dendrite spacing. Comparison of phase-field simulations with experimental observations. J Cryst Growth 237:149

[31] Ganesan M, Dye D, Lee P (2005) A technique for characterizing microsegregation in multicomponent alloys and its application to single-crystal superalloy castings. Metall Mater Trans A 36:2191

[32] Parsa AB, Wollgramm P, Buck H, Somsen C, Kostka A, Povstugar I, Choi PP et al (2015) Advanced scale bridging microstructure analysis of single crystal Ni-base superalloys. Adv Eng Mater 17:216

[33] Seo S, Lee J, Yoo Y, Jo C, Miyahara H, Ogi K (2011) A comparative study of the γ/γ'eutectic evolution during the solidification of Ni-base superalloys. Metall Mater Trans A 42:3150

[34] Eiken J, Apel M, Liang SM, Schmid-Fetzer R (2015) Impact of P and Sr on solidification sequence and morphology of hypoeutectic Al–Si alloys: combined thermodynamic computation and phase-field simulation. Acta Mater 98:152

[35] Higuchi K, Fecht HJ, Wunderlich RK (2010) Surface tension and viscosity of the Ni-based superalloy CMSX-4 measured by the oscillating drop method in parabolic flight experiments. Adv Eng Mater 9:349

[36] Elliott AJ, Pollock TM, Tin S, King WT, Huang SC, Gigliotti MFX (2004) Directional solidification of large superalloy castings with radiation and liquid-metal cooling: a comparative assessment. Metall Mater Trans A 35:3221

[37] Heckl A, Rettig R, Cenanovic S, Göken M, Singer R (2010) Investigation of the final stages of solidification and eutectic phase formation in Re and Ru containing nickel-base superalloys. J Cryst Growth 312:2137

[38] Tien J, Gamble R (1971) The suppression of dendritic growth in nickel-base superalloys during unidirectional solidification. Mater Sci Eng 8:152

[39] Beckermann C, Diepers H-J, Steinbach I, Karma A, Tong X (1999) Modeling melt convection in phase-field simulations of solidification. J Comput Phys 154:468

[40] Clarke AJ, Tourret D, Song Y, Imhoff SD, Gibbs PJ, Gibbs JW, Fezzaa K et al (2017) Microstructure selection in thin-sample directional solidification of an Al–Cu alloy: in situ X-ray imaging and phase-field simulations. Acta Mater 129:203

[41] Takaki T, Rojas R, Sakane S, Ohno M, Shibuta Y, Shimokawabe T, Aoki T (2017) Phase-field-lattice Boltzmann studies for dendritic growth with natural convection. J Cryst Growth 474:146

[42] Zhang H, Xu QY, Sun CB, Qi X, Tang N, Liu BC (2013) Simulation and experimental studies on grain selection behavior of single crystal superalloy II. Spiral part. Acta Metall Sin 49:1521

[43] Zhang H, Xu QY, Tang N, Pan D, Liu BC (2011) Numerical simulation of microstructure evolution during directional solidification process in directional solidified (DS) turbine blades. Sci China Technol Sci 54:3191

[44] Matan N, Cox D, Carter P, Rist M, Rae C, Reed R (1999) Creep of CMSX-4 superalloy single crystals: effects of misorientation and temperature. Acta Mater 47:1549

[45] Wang L, Liu Y, Yu J, Xu Y, Sun X, Guan H, Hu Z (2009) Orientation and temperature dependence of yielding and deformation behavior of a nickel-base single crystal superalloy. Mater Sci Eng A 505:144

[46] Liu B, Xu Q, Jing T, Shen H, Han Z (2011) Advances in multi-scale modeling of solidification and casting processes. JOM 63:19